Corrosion Science 53 (2011) 3712–3724

Contents lists available at ScienceDirect

Corrosion Science

journal homepage: www.elsevier.com/locate/corsci

Hot corrosion of a novel NiO/$NiFe_2O_4$ composite coating thermally converted from the electroplated Ni–Fe alloy

Li Ma [a], Kechao Zhou [a,*], Zhiyou Li [a], Qiuping Wei [b], Lei Zhang [a]

[a] State Key Laboratory of Powder Metallurgy, Central South University, Changsha 410083, PR China
[b] School of Materials Science and Engineering, Central South University, Changsha 410083, PR China

ARTICLE INFO

Article history:
Received 10 April 2011
Accepted 9 July 2011
Available online 20 July 2011

Keywords:
A. Metal coatings
A. Molten salts
B. SEM
C. Electrodeposited films
C. Hot corrosion
C. Oxidation

ABSTRACT

A novel NiO/$NiFe_2O_4$ composite coating thermally converted from an electroplated Ni–Fe alloy was successfully fabricated. The composite coating consisted of a NiO matrix and homogeneously distributed criss-cross intragranular and intergranular $NiFe_2O_4$ precipitates, with a very dense and flat structure. The composite, compared to bare Ni metal, exhibited increased hot corrosion resistance under an atmosphere of Na_3AlF_6–AlF_3–CaF molten salts and air at 960 °C, mainly because of the dense structure and well-adhered, homogeneously dispersed intragranular and intergranular $NiFe_2O_4$ precipitates.

1. Introduction

The spinel ferrites with general formula MFe_2O_4 have interesting physical properties and are of technological importance. In particular, $NiFe_2O_4$ is of increased interest as this material, in the form of bulk, powder, film, or nanoparticles, finds or promises numerous applications in microwave devices [1], magnetic drug delivery [2] and magnetic high-density data storage [3]. In addition, it has been found that $NiFe_2O_4$ is a highly reproducible material for humidity [4] and gas [5] sensing. Apart from its technological importance in these fields, $NiFe_2O_4$ has attracted considerable attention because of its potential for high temperature structural applications due to its low density, high strength at elevated temperature, good resistance to high temperature corrosion [6–9] and high electrical conductivity [6–11]. Most spinels have good conductivity and a coefficient of thermal expansion (CTE) that matches closely to those of other solid oxide fuel cell (SOFC) components [10,11]. Also, spinel coatings are effective barriers against chromium migration and evaporation [10,11]. Therefore, spinel oxides have been introduced as protective coatings for ferritic stainless steel interconnects in SOFCs [10,11]. In addition, spinels (e.g. $Ni_xFe_{3-x}O_4$) have also been considered to have potential as inert anode materials for aluminium electrolysis [6–8].

So far, a number of coating techniques have been utilised to synthesise spinel coatings, including pulsed laser deposition [12], sputtering [13], ferrite plating [14], dip coating [15], spray pyrolysis [16] and electroplating followed by thermal oxidation [10,17–19]. Among these methods, electroplating is very attractive due to the low cost of this process. Another important feature of electroplating is its capability to coat substrates with complex geometries, such as the SOFC interconnects with rectangular-shaped gas channels. As an emerging technology, composite electrodeposition is receiving increased interest because of its ability to produce films with many notable properties including high wear, oxidation and corrosion resistances, as well as remarkable electrical conductivity [20–23], which could be endowed electrodeposited alloy coatings with unique properties by incorporation of different second-phase ceramic nano-particles. Besides, upon heat treatment of the composite coatings, composite are formed which would be difficult or impossible to produce using conventional alloy electrodeposition methods, such as Co/$LaCrO_3$ [20] and Ni/$LaCrO_3$ [21]. It is well-known that the properties of composite coatings mainly depend on both the matrix phases and the amount and distribution of co-deposited particles. Sufficient incorporation percentages and more uniform distribution of fine inert particles in the metal matrix leads to the improvement of the mechanical, tribological, anti-corrosion, and anti-oxidation properties of the coatings. However, fine particles are easily agglomerated into larger particles in an electrolytic bath, leading to low particle contents and poor particle dispersion in the composite coating [22,23]. The similar phenomena have been observed in preparing Ni–Co–Fe_2O_3 composite coatings in our previous studies [24–27]. Besides, non-conducting ceramic particles (e.g. Fe_2O_3) also offer obstacles

* Corresponding author. Tel.: +86 731 88836264; fax: +86 731 88830464.
E-mail address: zhoukc2@mail.csu.edu.cn (K. Zhou).

0010-938X/$ - see front matter © 2011 Elsevier Ltd. All rights reserved.
doi:10.1016/j.corsci.2011.07.017

in achieving dense metal-ceramic (e.g. Ni–Fe_2O_3) interface during composite electroplating [24–27].

Accordingly, it is very necessary to seek for new techniques to solve above technique limitations for preparing composite coatings. Li and Fricoteaux et al. have proved that Ni–Fe alloys can be successful fabricated by alloy electrodeposition method [28,29]. Particularly, dense, smooth and homogeneous nano crystalline Ni–Fe alloy coatings can be prepared with a reasonably wide composition range by controlling the solution chemistry and deposition parameters [29]. If NiO/$NiFe_2O_4$ composite coatings could be thermally converted from an electroplated Ni–Fe alloy by thermal oxidation, it will solve the limitations of composite electrodeposition. However, elemental iron may be oxidised to many complex oxides during the oxidation process, such as FeO, Fe_2O_3 and Fe_3O_4. Pre-oxidation tests at 900–1200 °C for Ni–1–45%Fe (by wt.%) coatings were conducted in previous work, and showed that $NiFe_2O_4$ spinel could be formed for all alloy compositions [30]. However, only the oxide scales formed on the alloys containing 1–10%Fe (by wt.%) showed good adherence [30]. In addition, we observed that among Ni–1–10%Fe (by wt.%) alloys, the scales formed on Ni–7%Fe (by wt.%) coatings not only showed good adherence, but also displayed good oxidation resistance in air at 900–1200 °C [30]. Previous research has also indicated that spinels can be formed on alloys containing 4–25%Fe (by wt.%) after oxidation at 1000 °C [31]. However, it was observed that only the oxide scales formed on the alloys containing 2–10%Fe (by wt.%) showed good thermal shock resistance [31].

We have recently reported that NiO and $NiFe_2O_4$ have low solubility in Na_3AlF_6–AlF_3–CaF molten salts under standard aluminium reduction conditions [27]. It is expected that compounds in the NiO/$NiFe_2O_4$ system may exhibit good resistance to hot corrosion. Therefore, the aim of the present work is to fabricate Ni–7%Fe (by wt.%) coatings by an electroplating technique, followed by oxidation treatment to fabricate dense NiO–$NiFe_2O_4$ composite coatings with uniform phase distribution and microstructure, and to study the hot corrosion behaviour of these coatings at 960 °C (under standard aluminium reduction conditions in a mixture of Na_3AlF_6–AlF_3–CaF molten salts and air). The results may be useful for the application of this technologically important material.

2. Experimental

2.1. Electrodeposition

Pure nickel (99.5 %) specimens of dimensions 15 × 15 × 2 mm^3 were machined and grinded using SiC papers up to 800-grit finish, and then electroplated (on all sides) with a film of Ni–7%Fe (by wt.%) in an acid bath. The composition of the bath and electroplating parameters are presented in Table 1. The pH of the bath was adjusted to 3.5 by H_2SO_4. The substrates were sequentially ultrasonically cleaned in ethanol, acetone, and distilled water, each for 10 mins, then activated in an acidic solution (96 wt.% H_2SO_4:H_2O = 1:1 in volume) for 30 s, washed in distilled water, and finally immersed immediately in the plating bath for electrodeposition of the alloy coatings. The current density during deposition was adjusted to 5 A dm^{-2} with a deposition time of 120 mins.

2.2. Oxidation testing

Previous research has provided details of the formation of $NiFe_2O_4$ spinel by oxidation in air at 900–1200 °C on electroplated Ni–Fe alloy coatings [30]. Although the $NiFe_2O_4$ spinel phase can form at 900 °C, a temperature of 1200 °C is used as this hastens the process of oxidation treatment. In the present work, an oxidation treatment for the Ni–Fe-coated specimens and the bare Ni substrates was done at 1200 °C for 6 h in air.

2.3. Hot corrosion tests

The hot corrosion test method in the present study is similar to that previously applied to test (Ni,Co)O/(Ni,Co)Fe_2O_4 composite coatings [27]. This is briefly described here. Mixed Na_3AlF_6–AlF_3–CaF_2 powders were prepared with a Na_3AlF_6:AlF_3:CaF_2 mass ratio of 0.886:0.108:0.006 (standard solid electrolyte used for aluminium reduction; its melting temperature is 947 °C). The experimental apparatus is the same as that used in our previous work [27]. The pre-oxidised specimens and mixed salts were put into a large Al_2O_3 crucible, which was then placed in an electric vertical furnace. The test temperature was set to 960 °C (this is the traditional temperature used for aluminium reduction). To decrease experimental errors, all the specimens were the size (15 × 15 × 2 mm^3) and were placed in a radial symmetry. All the specimens were surrounded by an atmosphere consisting of a mixture of Na_3AlF_6–AlF_3–CaF_2 molten salt and air at 960 ± 5 °C. For comparison, the oxidised Ni–Fe coated specimens, the oxidised Ni substrate and the bare Ni substrates without the oxidation treatment were also tested under the same conditions. Following the corrosion test, the specimens were withdrawn from the Al_2O_3 plate and kept in air while the furnace was cooled to room temperature. The initial and final weights of the specimens exposed to the molten salt atmosphere and air were measured to assess the corrosion. At least three specimens of each type were corroded under the same conditions. The results presented here are representative of those found for all specimens subjected to a given parameter set.

2.4. Coating characterisation

The surface morphology of the electroplated, oxidation treated and corroded specimens were characterised by scanning electronic microscopy (SEM: JSM5600) and atomic force microscopy (AFM: Solver P47); their compositions were determined by energy dispersive X-ray spectroscopy (EDX: Oxford Link ISIS 300), and their structures were measured by X-ray diffraction (XRD: Rigaku/MAX-3A) with Cu K_α radiation (λ = 0.154 nm, scanning rate: 4° per minute) and Raman spectroscopy (LabRAM HR800) at an

Table 1
Solutions composition and conditions for Ni–Fe alloy electroplating.

Electrolyte ingredients	Concentration (g/L)	Plating parameters
Nickel sulphate ($NiSO_4·6H_2O$)	250	pH: 3.5 ± 0.1
Nickel Chloride ($NiCl_2·6H_2O$)	45	Temperature (°C): 55 ± 3
Ferrous sulphate ($FeSO_4·7H_2O$)	8	Current density (A dm^{-2}): 5
Boric acid (H_3BO_3)	35	Deposition time (min): 120
Sodium citrate ($Na_3C_6H_5O_7·2H_2O$)	20	
Sodium dodecylsulfate ($C_{12}H_{25}SO_4Na$)	0.2	
Saccharin ($C_7H_5O_3NS$)	3	
Sodium benzenesulfinate ($C_6H_5NaO_2S$)	0.2	

excitation wavelength of 488 nm (argon ion laser, output power of 100 mW).

3. Results and discussion

3.1. Morphologies and phase structure of as-electroplated Ni–Fe alloy

XRD patterns of the Ni substrate and the as-deposited Ni–Fe coating on a Ni substrate are shown in Fig. 1(a) and (b) respectively. The XRD patterns of the Ni substrate (Fig. 1(a)) and the Ni–Fe coating deposited on the Ni substrate (Fig. 1(b)) reveal that the electroplated Ni–Fe alloy coating is a solid solution. A clear preferred orientation in the (100) crystallographic direction can be observed. The diffraction peaks of the (111), (200) and (220) planes are all shifted to smaller 2θ values (shown in the insets to Fig. 1(b)), due to incorporation of iron atoms in the nickel lattice. Broadening of the (200) and (111) diffraction peaks can be also observed, indicating that the grain size of the Ni–Fe coating is small.

The AFM surface morphology, cross-section morphology, and the EDX analysis of the as-deposited Ni–Fe alloy coating are shown in Fig. 2. In Fig. 2(a) and (b), the surface of as-deposited Ni–Fe alloy coating is very compact and smooth, whereas that of as-deposited Ni–Co–Fe_2O_3 composite coating by composite electrodeposition was very rough and spallation of some fresh deposits have been observed on the surface [27]. Besides, it can be also seen that the average grain size of the as-electroplated Ni–Fe coating is much smaller than 100 nm. The electroplated Ni–Fe layer was continuous and dense with an average thickness of about 170 μm, and was well bonded to the Ni substrate (Fig. 2(b)). However, for the as-deposited Ni–Co–Fe_2O_3 composite coating in our previous study, some pores could be observed in the interface of the coating and Ni substrate [27]. Analysis by EDX (Fig. 2(c)) indicated that the Ni and Fe content of the Ni–Fe layer was about 93% and 7% (by wt.%), respectively. The composition of the as-electroplated Ni–Fe layer is close to that of Ni–(2–10%)Fe (by wt.%) alloys on which $(Fe,Ni)_3O_4$ spinel oxide phase was formed after heating in air at 1000 °C [31].

3.2. Oxidation treatment

3.2.1. XRD and Raman analyses of the oxide scales

Fig. 3 shows the XRD patterns of the Ni substrate and the Ni–Fe alloy coated specimen after oxidation at 1200 °C for 6 h and then cooled in air. The phase composition of the oxidised Ni substrate, determined by XRD, was Ni and NiO (Fig. 3(a)), while that of the oxidised Ni–Fe coated specimen was (Ni,Fe)O and $NiFe_2O_4$ (Fig. 3(b)). The formation of $NiFe_2O_4$ can be clearly seen in the right insert of Fig. 3(b). Note that the peak at 2θ ~43.361° is very strong compared with the other peaks, indicating highly preferential crystal growth along the (100) direction. In the left insert, it can be seen that this peak actually consists of two peaks, matching the NiO (200) peak at 43.275° and the $NiFe_2O_4$ (400) peak at 43.373°. The peak intensities of NiO (200) and $NiFe_2O_4$ (400) are both very strong compared with their other peaks. Thus, the NiO and $NiFe_2O_4$ phases thermally grown on the Ni–Fe coating have the same strong (100) orientation. However, the (200), (111) and (220) peaks of NiO (JCPDF 73-1523) have nearly the same 2θ values as those of the (400), (222) and (440) peaks of $NiFe_2O_4$ (JCPDF 74-1913), so the texture coefficients of NiO or $NiFe_2O_4$ cannot be calculated from the XRD results. As for pre-oxidised Ni–Co–Fe_2O_3 coating in the previous study [27], almost no preferred orientation was found in its scale.

The formation of $NiFe_2O_4$ was further confirmed by Raman spectroscopy. The Raman spectra obtained from the external parts of the oxide scales at five different positions on the Ni–Fe coating formed during oxidation at 1200 °C for 6 h are shown in Fig. 4(b)–(f). The Raman spectra of the oxide scale formed on the Ni substrate during oxidation at 1200 °C for 6 h is also included for comparison (Fig. 4(a)). The main features of the spectra of the oxides formed on Ni–Fe coating (Fig. 4(b)–(f)) are obviously different from those of the oxide formed on the Ni substrate. The spectra oxide formed on the pure Ni substrate (Fig. 4(a)) shows bands at 416, 501, 547, 733, 902, 1095, 1495 cm^{-1}, which are indicative of NiO phase [32,33]. The oxide formed on Ni–Fe coated specimen shows Raman peaks at 212, 332, 485, 578, 660 (shoulder) and 701 cm^{-1} (Fig. 4(b)–(f)), which are assigned to the $NiFe_2O_4$ crystal phase [32,34]. However, the other peaks for the oxide on the Ni–Fe coatings (Fig. 4(b)–(f)), such as the peaks at 380 and 860–895, 1095–1105 and 1485–1495 cm^{-1}, are considered to be due to NiO phase. Thus, the Raman and XRD investigations of the oxide scale surface confirm the presence of both spinel and NiO phases. The spectra of the oxide scale on the Ni–Fe coating do not change significantly from place to place on the sample surface (Fig. 4(b)–(f)). This indicates a homogeneous composition of the layer at the micrometre scale, since previous research has shown that the Raman probe analysis depth in oxide films on metals or alloys is smaller than 1 μm [33,35]. Furthermore, this result indicates that the $NiFe_2O_4$ phase spatial density was very high. However, the Fe content of the alloy was only 7% (by wt.%), so the weight percentage of the

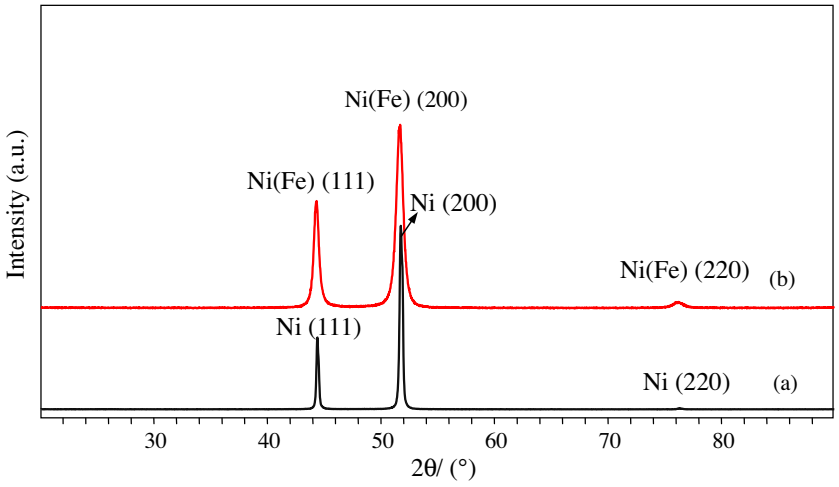

Fig. 1. XRD patterns of (a) the Ni metal substrate and (b) as-deposited Ni–Fe coating on a Ni substrate.

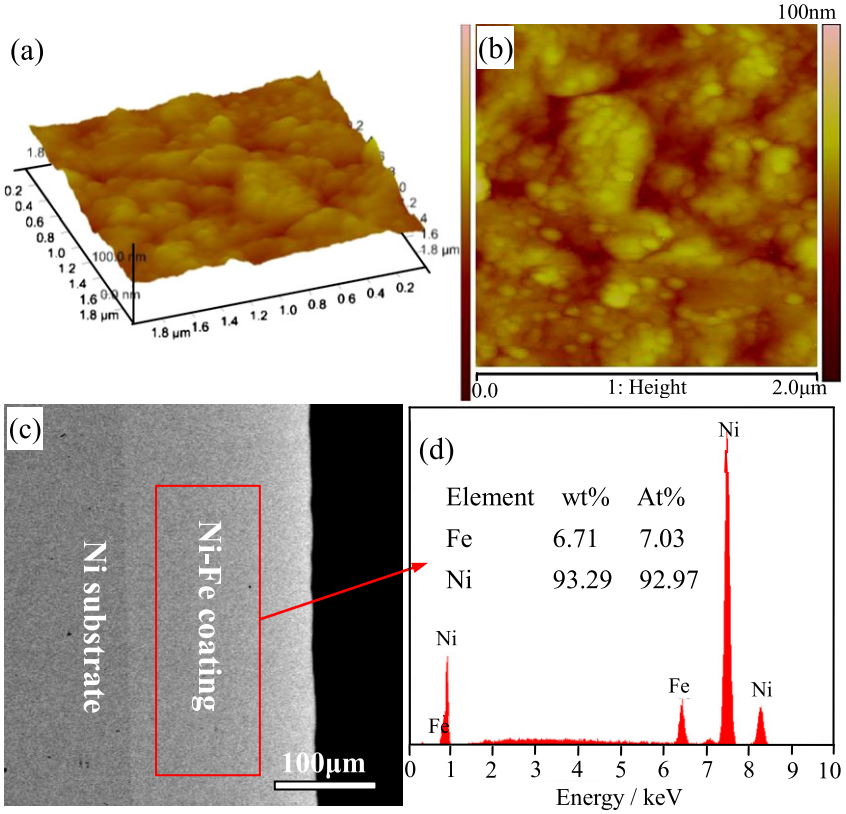

Fig. 2. The surface AFM images (a) and (b), cross-section (b) and EDX analyses (c) of as-deposited Ni–Fe coating on a Ni substrate.

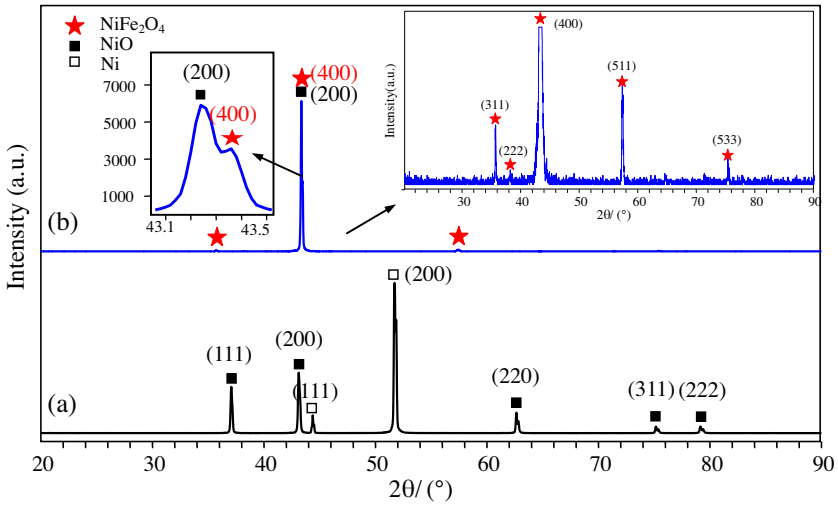

Fig. 3. XRD patterns of the oxide scales formed on (a) the Ni substrate and (b) the Ni–Fe alloy coating after oxidation at 1200 °C for 6 h in air. The inset shows the detailed view of the selected regions of the XRD pattern.

$NiFe_2O_4$ phase formed in the oxide scale is very low. From these results, it can be deduced that the crystal size of the $NiFe_2O_4$ phase was very small, but the number of the $NiFe_2O_4$ spinel crystals was large.

3.2.2. SEM/EDX analyses of the oxide scales formed at 1200 °C

Images of the surface and X-ray maps of the Ni–Fe alloy coated specimen after oxidation at 1200 °C for 6 h are shown in Figs. 5 and 6, respectively. The surface of the pre-oxidised Ni–Fe alloy coating is surprisingly flat and has no hole or crack (Fig. 5(a)), whereas that of the pre-oxidised Ni–Co–Fe_2O_3 composite coating in the previous study was uneven and had some pores [27]. Besides, many nanometre-sized criss-cross intragranular precipitates are distributed homogeneously on the surface of the oxide scale (Fig. 5(b)), which is in good agreement with the Raman results. The Point-count EDX spectra (Fig. 5(c) and (d)) and EDX maps (Fig. 6) indicate that these are Fe-rich oxide. An O- and Ni-rich oxide was detected in the flat areas. EDX analysis of point A indicates a small amount of Fe was also detected in the flat areas. Previous studies of Fe–Ni–O systems at 1200 °C have shown that the maximum solubility of iron in

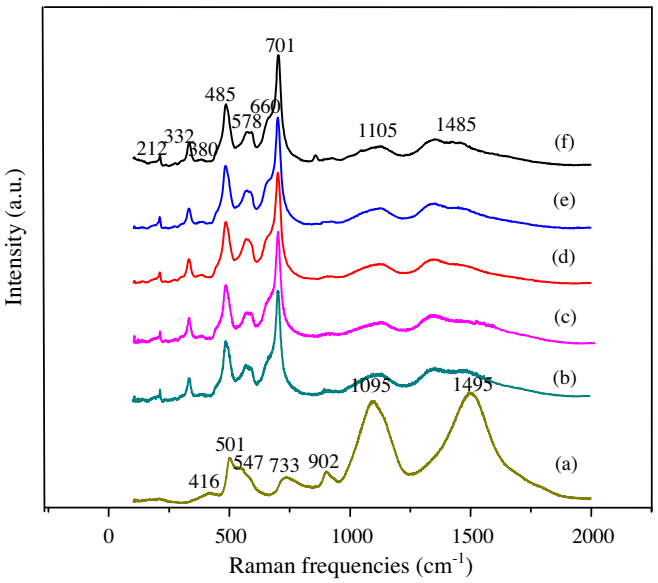

Fig. 4. Raman patterns of the oxide scales formed on (a) the Ni substrate pre-oxidised at 1200 °C for 6 h; (b), (c), (d), (e) and (f) the Ni–Fe coated specimen pre-oxidised at 1200 °C for 6 h recorded from five different points on the top scale surface.

bunsenite (Ni,Fe)O is 0.16 mol fraction [36]. Based on the XRD, Raman and EDX analyses, the criss-cross intragranular precipitates are likely to be $NiFe_2O_4$ spinel, while the O/Ni-rich oxide is likely to be NiO. The $NiFe_2O_4$ spinel phase precipitated due to the low solubility of Fe^{3+} in NiO [37]. It is worth noting that the spinel precipitates seem to be preferentially distributed along the {001} planes, i.e. (001) and (010), of the host grain of (Ni,Fe)O (Fig. 5(b)), in agreement with the XRD results (Fig. 3(b)). The {001} habit-plane selection of parallel-epitaxial spinel could be related to minimization of the coherency strain energy across the interface of (Ni,Fe)O and its $2 \times 2 \times 2$ superlattice, i.e. the $NiFe_2O_4$ spinel nanocrystalline. The grown spinel plate with a {100} habit plane has been previously observed for $NiFe_2O_4$ in NiO [38]. In addition, many intergranular precipitates along NiO grain boundaries were observed (Figs. 5 and 6). Based on the XRD and Raman analyses, these intergranular precipitates are also likely to be $NiFe_2O_4$ spinel. The smooth surfaces and uniform nanostructures of the crack-free dense coatings will have broad application prospects in machinery and other areas.

The cross-section morphologies of the Ni–Fe coated specimen pre-oxidised at 1200 °C for 6 h were also investigated by SEM (Fig. 7). The SEM images show that an adherent, dense and homogeneous oxide scale with a thickness of ~170 μm has formed. The oxide scales showed good adherence with no tendency to delaminate from the substrate. Moreover, criss-cross intragranular precipitates were also detected on the cross-section of the scale, consistent with the formation of the $NiFe_2O_4$ intragranular precipitates on the oxide surface (Fig. 5(b)).

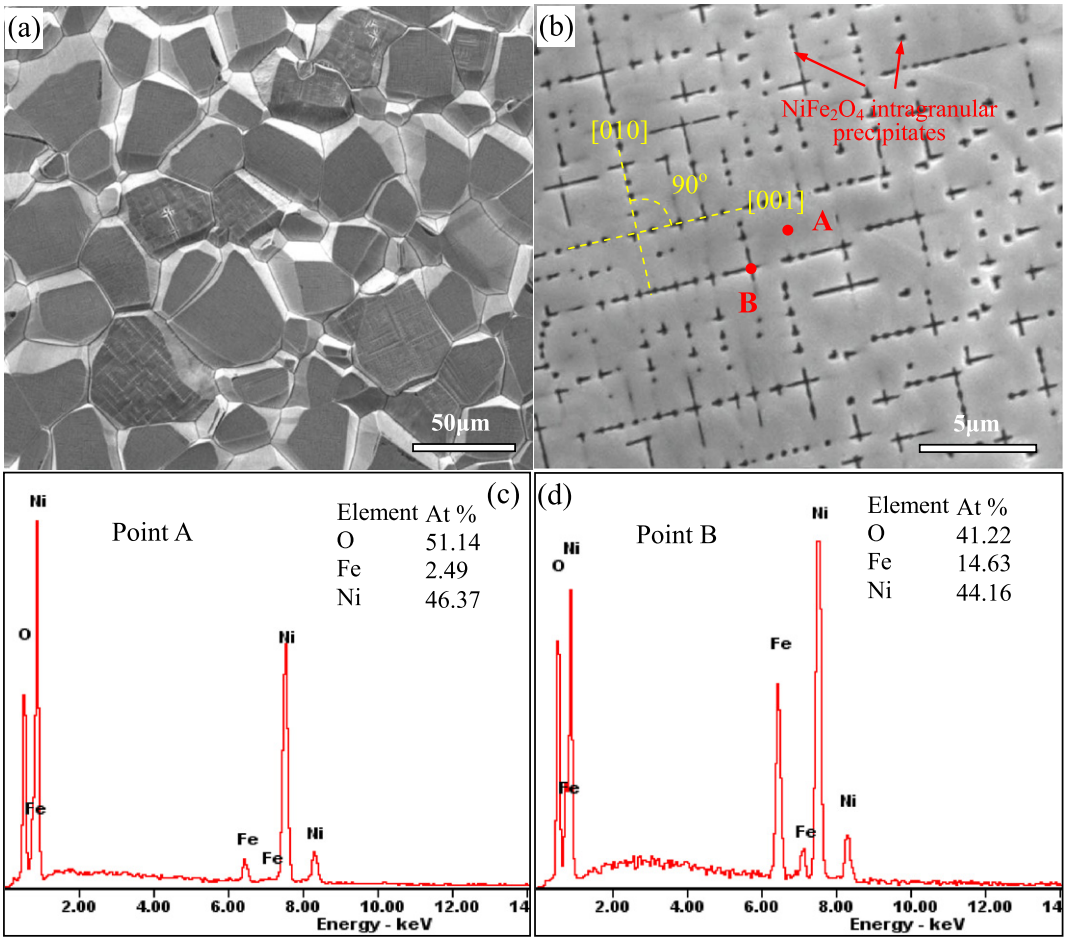

Fig. 5. The surface morphology and EDX analyses of the Ni–Fe coated specimen pre-oxidised at 1200 °C for 6 h (a) the surface morphology; (b) an enlarged view of Fig. 5(a); (c) and (d) the corresponding EDX analyses of point A and B in Fig. 5(b).

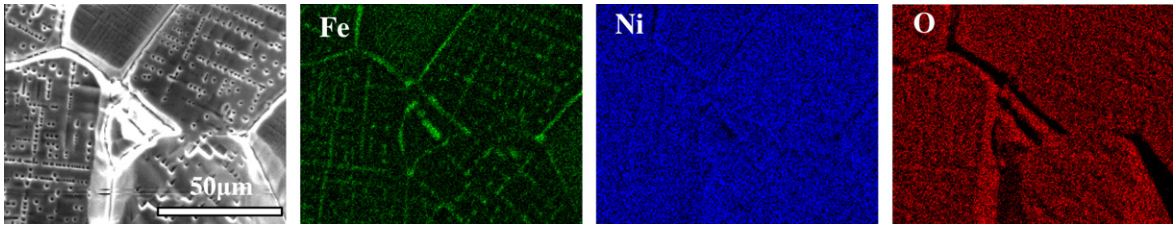

Fig. 6. EDX maps of a portion of the Ni–Fe coated specimen pre-oxidised at 1200 °C for 6 h.

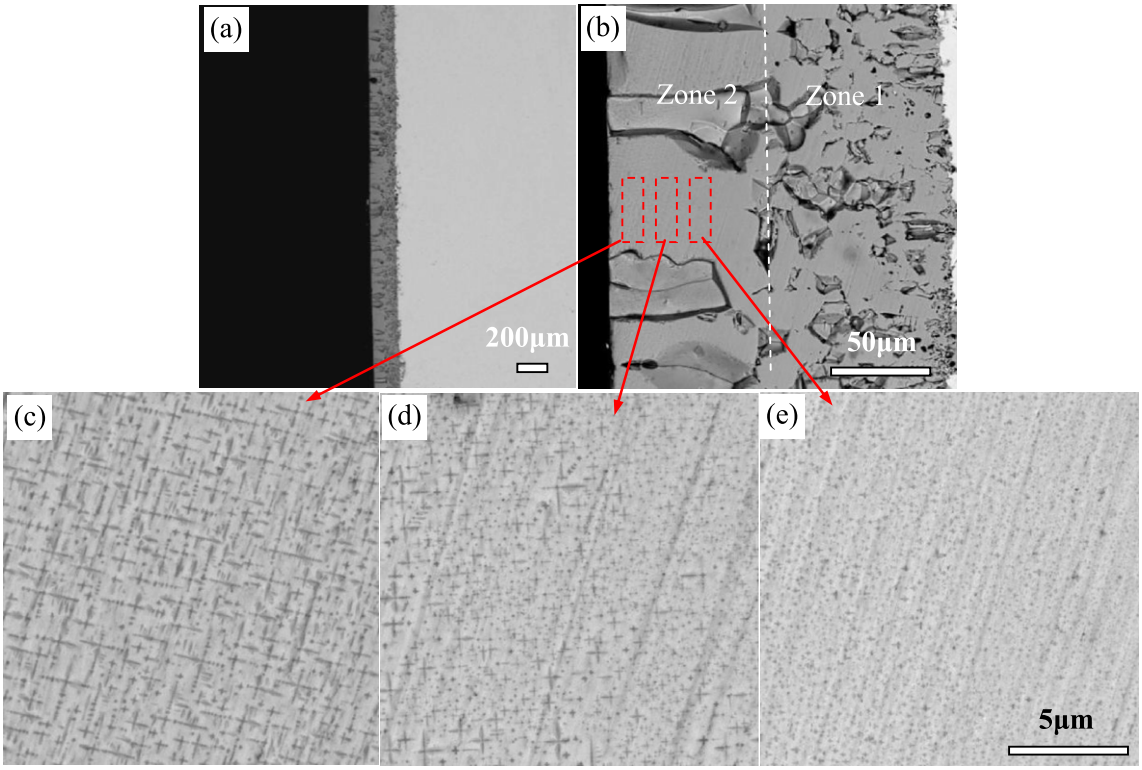

Fig. 7. (a), (b) Cross-section SEM images of the Ni–Fe coated specimen pre-oxidised at 1200 °C for 6 h; (c), (d) and (e) show the selected regions of the SEM images at higher magnifications.

The scale on the Ni–Fe alloy coating structurally consisted of two zones (Fig. 7(b)). A zone containing small equiaxed grains, which exhibited a remarkably sharp boundary, existed at the alloy/oxide interface (zone 1). Beyond this boundary a zone of larger columnar grains with many small intergranular and intragranular spinel precipitates extending up to the oxide/gas interface was observed (zone 2). The number and size of the intragranular precipitates decreased from the gas/oxide interface to the oxide/alloy interface. The explanation for this is as follows. Iron preferentially concentrates towards the outer surface of the nickel oxide in the form of spinel intragranular precipitates as reported in [39]. The value of oxygen activity decreases from the outer oxide surface to the bulk alloy, as required from thermodynamic considerations. At very low oxygen potentials, iron in nickel oxide is present in the form of ferrous ions. Since this does not require creation of additional vacancies, solubility of iron in this oxide is high at low oxygen potentials. Iron tends to pass from the ferrous to the ferric state with increasing oxygen potential. Since NiO cannot incorporate ferric iron in large concentrations without sustaining a high concentration of vacancies, the iron solubility rapidly decreases with increasing oxygen pressure [40]. Iron solubility in nickel oxide is negligible at $PO_2 \sim 1$ atm, and correspondingly iron is preferentially concentrated in the spinel phase which can accommodate ferric ion easily in its crystal lattice [40]. Consequently, the concentration and size of the spinel intragranular precipitate increased gradually towards the interface between the oxide scale and the gas, as seen in Fig. 7(c)–(e). The gradient distribution in the direction perpendicular to the oxide scale surface is beneficial to the adhesion of the oxide scale. What's more, the high spinel content in the outer zone is also beneficial to the electrical conductivity at high temperatures. Thus, it can be used for electric interconnects at high temperature; such as ferritic stainless steel interconnects in SOFCs and the current anode interconnects for aluminium reduction, because of the high conductivity of the mixed iron–nickel oxides [17,41] ($NiFe_2O_4$ electrical conductivity is $\sim 0.26\ S\ cm^{-1}$ at 800 °C [42]), and the good chemical stability of $Ni_xFe_{3-x}O_4$ spinels at high temperature [8–10,17,18]. However, for those pre-oxidised Ni–Co–Fe_2O_3 composite coatings reported in the previous work [27], the cross-section morphologies were very different to the present work, few spinel nanoparticles distributed unhomogeneously in the surface was observed. Besides, spinel nanoparticles with gradient distribution throughout the thickness were not found.

3.3. Corrosion behaviour

3.3.1. Mass gain

The weight gains of the bare, the pre-oxidised Ni substrates and the pre-oxidised Ni–Co–Fe_2O_3 coated specimens in previous study [27] as well as the pre-oxidised Ni–Fe composite coated specimen

after the corrosion tests in an atmosphere of Na_3AlF_6–AlF_3–CaF molten salts and air at 960 °C are shown in Fig. 8. For the bare and pre-oxidised Ni substrates, the mass changed significantly during hot corrosion, and their final average mass gains were ~6.0 mg cm^{-2} and ~5.0 mg cm^{-2} after only 15 h corrosion, respectively. For the pre-oxidised Ni–Co–Fe_2O_3 coated specimens, their mass gains were lower than the bare and pre-oxidised Ni substrates, and their average mass gains were ~1.8 mg cm^{-2} and ~3.5 mg cm^{-2} after 15 h and 30 h corrosion, respectively. The previous studies have revealed that the pre-oxidised Ni–Co–Fe_2O_3 coated specimens show better corrosion resistance than the bare and pre-oxidised Ni substrates, and that the bare and pre-oxidised Ni substrates suffer serious corrosion attack because they have no protective scales [27]. However, for the pre-oxidised Ni–Fe coated specimens, only small mass gains (~0.5 mg cm^{-2}) after corrosion for 15 h were observed. After corrosion for 30 h, the average mass gain was also clearly lower (~1.5 mg cm^{-2}) than that of the bare or pre-oxidised Ni substrates or pre-oxidised Ni–Co–Fe_2O_3 coated specimens corroded for 15 h. As corrosion continued for up to 50 h, the average mass gain was still clearly lower than 2.5 mg cm^{-2}. Thus, the pre-oxidised Ni–Fe coated specimens show lower weight gains than the pre-oxidised Ni–Co–Fe_2O_3 coated specimens.

Therefore, compared to the bare or pre-oxidised Ni substrates or pre-oxidised Ni–Co–Fe_2O_3 coated specimens, the mass change of the pre-oxidised Ni–Fe coated specimens was very small in an oxidising Na_3AlF_6–AlF_3–CaF molten salt atomsphere, indicating that the pre-oxidised Ni–Fe coated specimens have superior corrosion resistance and chemical and thermal stability under these conditions.

3.3.2. XRD analysis of the hot corrosion products

The XRD patterns of the Ni–Fe coated specimen pre-oxidised at 1200 °C for 6 h and then corroded for 15, 30 and 50 h at 960 °C are shown in Fig. 9(b)–(d), respectively. For comparison, the XRD pattern of the bare Ni substrate after corrosion for 15 h at 960 °C is shown in Fig. 9(a). The main phases identified for the corroded Ni coated specimens are NiO and $NiAl_2O_4$. The hot corroded oxidised Ni–Fe coated specimen contains phases such as NiO, $NiFe_2O_4$ and (Ni,Fe)Al_2O_4. With increasing corrosion time, the intensity of the (Ni,Fe)Al_2O_4 spinel peaks increased, due to the difference in the (Ni,Fe)Al_2O_4, $NiFe_2O_4$ and (Ni,Fe)O concentration of the scale with different corrosion time. (Ni,Fe)Al_2O_4 spinel may be formed by chemical reaction between AlF_3 in the atmosphere and the oxide scale. The large I(200)/I(111) or I(400)/I(222) ratio in Fig. 9(d) corresponding to NiO and $NiFe_2O_4$ indicates that the strong (100) texture of the oxide scale on the Ni–Fe alloy coating still existed after a 50 h of corrosion.

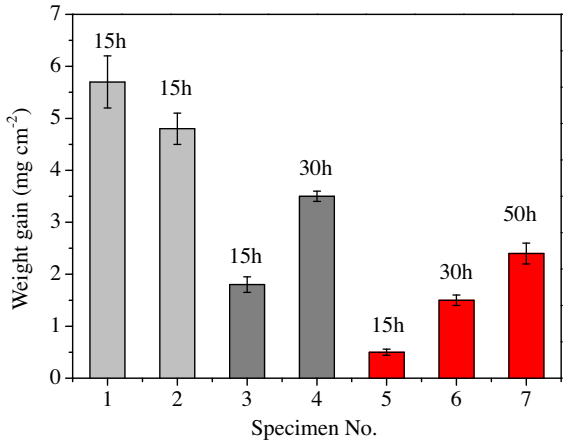

Fig. 8. Weight gains of the bare Ni substrates [27], pre-oxidised Ni [27], the pre-oxidised Ni–Co–Fe_2O_3 [27] coated specimens and the oxidised Ni–Fe coated specimens corroded at 960 °C for different hours (1: Ni substrates; 2: pre-oxidised Ni; 3 and 4: pre-oxidised Ni–Co–Fe_2O_3 coated specimens; 5, 6 and 7: the pre-oxidised Ni–Fe coated specimens).

It is noted that for the untreated pure Ni samples, molten salts (mainly Na_3AlF_6 and CaF_2) were detected in XRD analysis of the scale after corrosion at 960 °C for 15 h (Fig. 9(a)). It has been observed in our previous studies [27] that the molten salts penetrated through the scale. However, the diffraction peaks for the molten salts were barely visible in the XRD patterns of the pre-oxidised Ni–Fe coated samples after corrosion, suggesting that the amounts of these salts present was very small. This difference can be attributed to the presence of a protective scale with a dense structure formed during the oxidation treatment, which could prevent the penetration of salts into the scale.

3.3.3. SEM/EDX analyses of the hot corrosion products at 960 °C

Fig. 10(a)–(c) show the surface morphologies of the Ni–Fe coated specimen pre-oxidised at 1200 °C for 6 h and then corroded for 15, 30 and 50 h at 960 °C, respectively. The surfaces of all of the pre-oxidised specimens before and after corrosion tests are free of cracks, and the oxide scale was conserved in all cases, indicating that the oxide scale has high resistance to the molten salts. After corrosion for 15 h, the surfaces of the pre-oxidised specimens are still flat. However, for those pre-oxidised Ni–Co–Fe_2O_3 composite coatings reported in the previous work [27], their surfaces after corrosion for 15 h were very uneven, and a few spalled regions could be observed. After corrosion for 30 h and 50 h, many large lace-like oxide ridges were formed along the grain boundaries of the pre-oxidised Ni–Fe specimens. Thus, for the Ni–Fe coated specimen pre-oxidised at 1200 °C for 6 h and then corroded for 50 h at 960 °C, the surface morphology consisted of two regions: M is the flat surface; N is oxide ridges along the grain boundaries. Fig. 10(d) shows the AFM image of the flat surface of the Ni–Fe coated specimen pre-oxidised at 1200 °C for 6 h and then corroded for 50 h at 960 °C. It can be seen from Fig. 10(d) that the flat surface of the sample corroded at 960 °C consisted of a number of small pyramid crystallites. The corresponding EDX spectra of region M and N are shown in Fig. 10(e) and (f), respectively. EDX analysis reveals that region M is rich in Ni, Al, and O with a small amount of Fe. Combining the results of XRD and EDX, we conclude that region M mainly consisted of $NiAl_2O_4$. In region N, EDX analysis identifies the main elements present again to be Ni, Al, and O. Combining the results of XRD and EDX, strong Al peaks in region N were due to the presence of $NiAl_2O_4$, which existed under the corrosion products. Therefore, it is reasonable to conclude that the main phase in this area was $NiAl_2O_4$. The main corrosion product $NiAl_2O_4$ was similar to that in pre-oxidised Ni–Co–Fe_2O_3 composite coatings [27]. With increasing corrosion time, the amount of lace-like oxide ridges along the grain boundaries increased, consistent with the XRD results (Fig. 10).

The explanation for the formation of the lace-like oxide ridges along the grain boundaries is as follows. When the salt contaminants combine together to form molten deposits at high temperature, the scale is in direct contact with the salts. The grain boundaries, like grooves or gutters, are more easily filled with molten salts, compared with the flat and smooth surface areas. Fig. 11 shows the surface morphology and the corresponding EDX spectrum of the Ni–Fe coated specimen pre-oxidised at 1200 °C for 6 h and then corroded for 15 h at 960 °C. Molten salt can be observed along the grain boundaries of the oxide scale after hot corrosion. Thus, large corrosion products are formed along the grain boundaries due to the large mass of reaction medium supplied in those areas throughout the hot corrosion process. A model of these reactions is shown in Fig. 12.

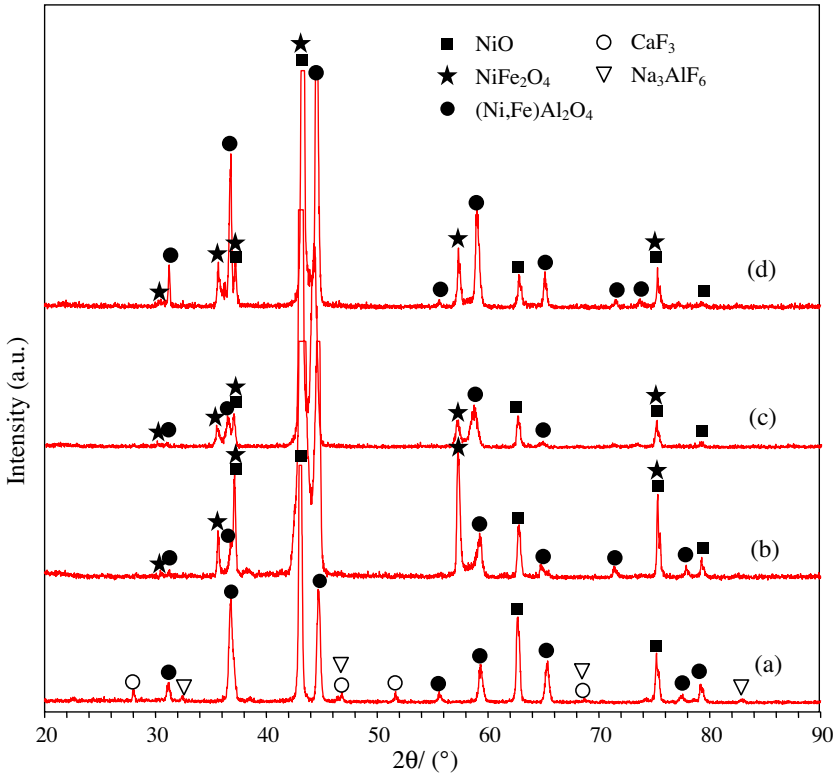

Fig. 9. XRD patterns for the hot corroded surfaces of (a) the bare Ni substrates, (b), (c), and (d) pre-oxidised Ni–Fe coated specimens exposed to an atmosphere of molten Na_3AlF_6–AlF_3–CaF_2 salts and air at 960 °C ((a) and (b): corrosion for 15 h; (c): corrosion for 30 h; (d): corrosion for 50 h).

Fig. 13 shows the cross-section morphology of the Ni–Fe coated specimen pre-oxidised at 1200 °C for 6 h and then corroded for 15, 30 and 50 h at 960 °C. All of the oxide scales were well-adhered to the substrate, and the thickness increased slightly as the corrosion time increased. After 50 h of corrosion, the thickness of the oxide layer had increased by only ~40 μm compared with that of the pre-oxidised Ni–Fe coated specimen (Fig. 7(b)), which was similar to that of (Ni,Co)O/(Ni,Co)Fe_2O_4 composite coating after corrosion for only 30 h in the previous study [27]. This implies that the pre-oxidised Ni–Fe coating provided better protection against corrosion by air and molten salts. Furthermore, no molten salt was observed in the scale, indicating that the pre-formed scale with a dense structure was able to prevent the penetration of salts into the scale. For all Ni–Fe coated specimens in every corrosion test, a new thin layer of (Ni,Fe)Al_2O_4 (~3–5 μm) was formed next to the layer of NiO and spinel phases that was formed during the oxidation treatment. As the corrosion time increased, the thickness of this (Ni,Fe)Al_2O_4 layer increased slightly, which was also similar to that of (Ni,Co)O/(Ni,Co)Fe_2O_4 composite coating [27].

More detailed images of the cross-section of the oxide scale after corrosion for 15, 30 and 50 h are shown in Fig. 14. Beyond 15 h of corrosion at 960 °C, there is an apparent decrease in the density of the $NiFe_2O_4$ intergranular precipitates and thus an apparent increase in the average precipitate size. This may be due to the volume fraction of precipitate quickly reaching its maximum value; the precipitates then grow at the expense of smaller particles [43,44]. In other words, once the amount of the precipitate has reached its maximum value, the only process that occurs as the corrosion test continues is coalescence of the precipitates. The driving force for this coalescence is the lowering of the total interfacial energy of the system [44]. A high concentration of Fe is observed along the columnar NiO grains boundaries just below the $NiAl_2O_4$ scale. The same phenomenon was also observed on the surface of the pre-oxidised Ni–Fe coated specimen (Fig. 5). This suggests that the diffusivity of Fe is fast at the grain boundaries of the oxidised Ni–Fe coated specimen, which promotes the formation of intergranular $NiFe_2O_4$ spinel precipitates along the columnar NiO grain boundaries. An enlarged image of the cross-section of the oxide scale after corrosion for 50 h is shown in Fig. 15. The scales on the Ni–Fe coatings consisted of three zones with different compositions (Fig. 15). After corrosion, there is now a third zone (Zone 3) in addition to the two zones (Fig. 7(b)) discussed earlier. The third zone (Zone 3) consisted of (Ni,Fe)Al_2O_4 phase extending up to the oxide/gas interface was observed (Zone 3).

As found in previous studies [27], for the bare nickel substrate, the scale formed on the surface easily spalled off during hot corrosion, mainly because thermal stresses could develop during cooling due to the difference of coefficient of thermal expansion (CTE) between the NiO ($17.1 \times 10^{-6}\ K^{-1}$) [42] and the $NiAl_2O_4$ ($8.1 \times 10^{-6}\ K^{-1}$) [42]. In contrast, for all the pre-oxidised Ni–Fe coated samples, the surface of the oxide scale was intact after the corrosion test and the oxide scale was well-adhered to the substrate, indicating strong bonding not only between the (Ni,Fe)Al_2O_4 layer and the (Ni,Fe)O + spinel layer, but also between the nickel substrate and the oxide scale. Since the CTE value of $NiFe_2O_4$ is between those of NiO and $NiAl_2O_4$ ($NiFe_2O_4$ ~$10.8 \times 10^{-6}\ K^{-1}$ [42]), the thermal stress between the NiO and $NiAl_2O_4$ phases is reduced by incorporation of $NiFe_2O_4$ particles in the columnar NiO matrix. In addition, previous transmission electron microscopic investigations on the NiO/$NiFe_2O_4$ interface have shown that $NiFe_2O_4$ and NiO share close crystallographic relations and have low lattice mismatch, which results in small lattice distortion [38]. In other words, the scale formed during oxidation treatment has good compatibility with the nickel substrate, which increases the stability of the oxide scale. Furthermore, the concentration of $NiFe_2O_4$ particles increased gradually from the nickel/oxide interface to the oxide/gas interface

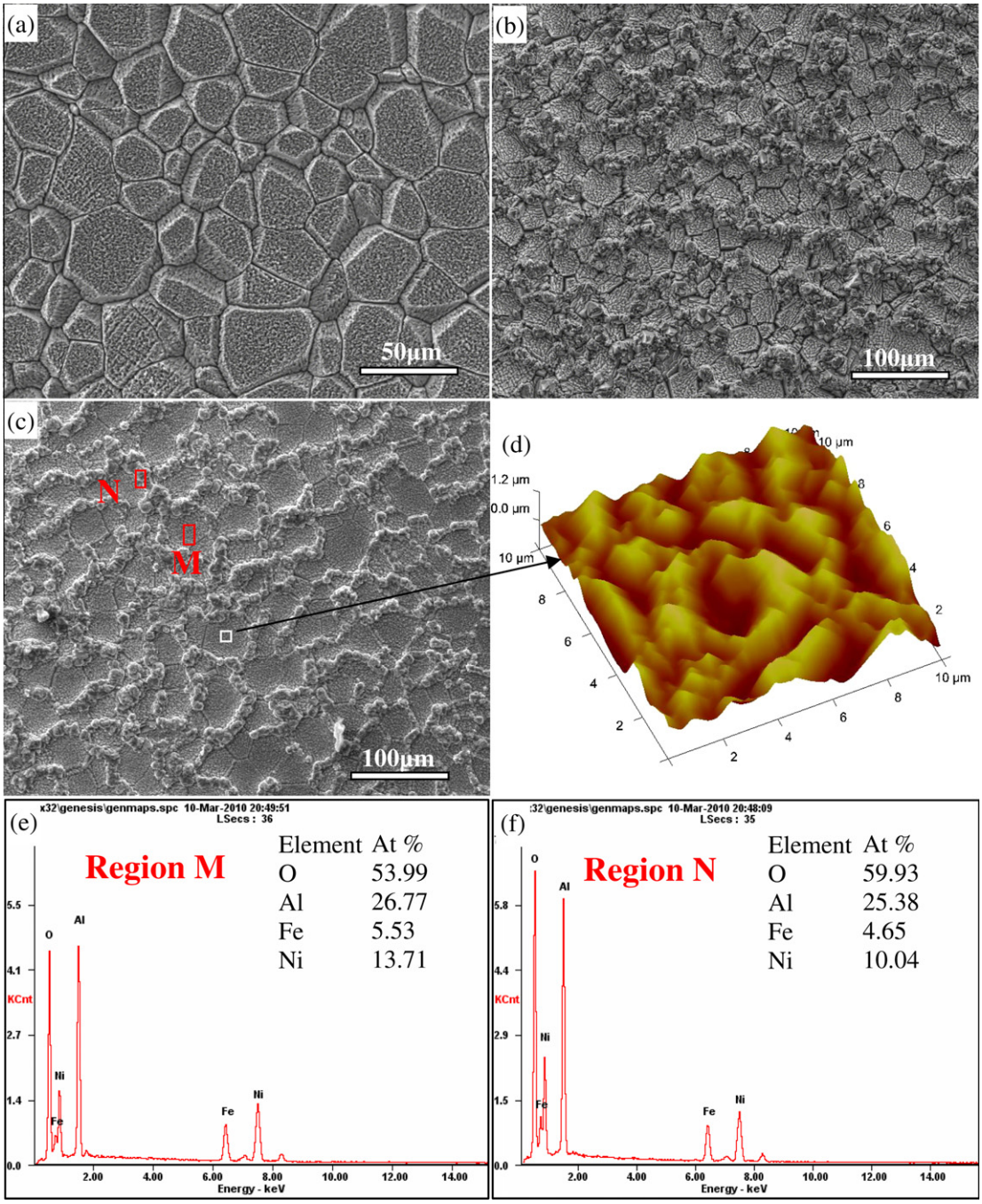

Fig. 10. SEM micrographs of the surface-scales formed on the pre-oxidised Ni–Fe coated specimens after hot corrosion at 960 °C ((a): corrosion for 15 h; (b): corrosion for 30 h; (c): corrosion for 50 h); (d) surface AFM image of the pre-oxidised Ni–Fe coated specimen after hot corrosion at 960 °C for 50 h; (e) and (f) EDX analysis of the Ni–Fe coated specimen pre-oxidised at 1200 °C for 6 h and then corroded for 50 h at 960 °C corresponding to surface SEM image.

(Fig. 7), which also helps to reduce the thermal stress between the NiO and $NiAl_2O_4$ phases.

3.4. Corrosion resistance of the coatings

The $(Ni,Fe)Al_2O_4$ scale was formed on the surface of the two coatings in the present work and the reference [27] in the initial corrosion stage and acted as a barrier layer to separate the coating from the aggressive environment. However, their generation mechanisms are different. The formation of $(Ni,Co,Fe)Al_2O_4$ layers during the corrosion test in the previous work had been discussed in the literature of [27]. However, the formation of $(Ni,Fe)Al_2O_4$ layers during the corrosion test in the present work was mainly due to the following reasons.

Although NiO, Fe_2O_3, $NiFe_2O_4$ have been used as inert anode materials, they all have low solubility in molten salts [45]. The results presented in this paper have demonstrated that the pre-oxidation treatment resulted in the formation of a dense and continuous scale mainly composed of (Ni,Fe)O and $NiFe_2O_4$ (Fig. 5(c)). Thus, the probable dissolution reactions are (1) [46] and (2) [47]:

$$NiFe_2O_4(s) + 2AlF_3(l) \rightarrow NiO + 2FeF_3(l) + Al_2O_3(l) \quad (1)$$

$$3NiO(s) + 2AlF_3(l) \rightarrow 3NiF_2(l) + Al_2O_3(l) \quad (2)$$

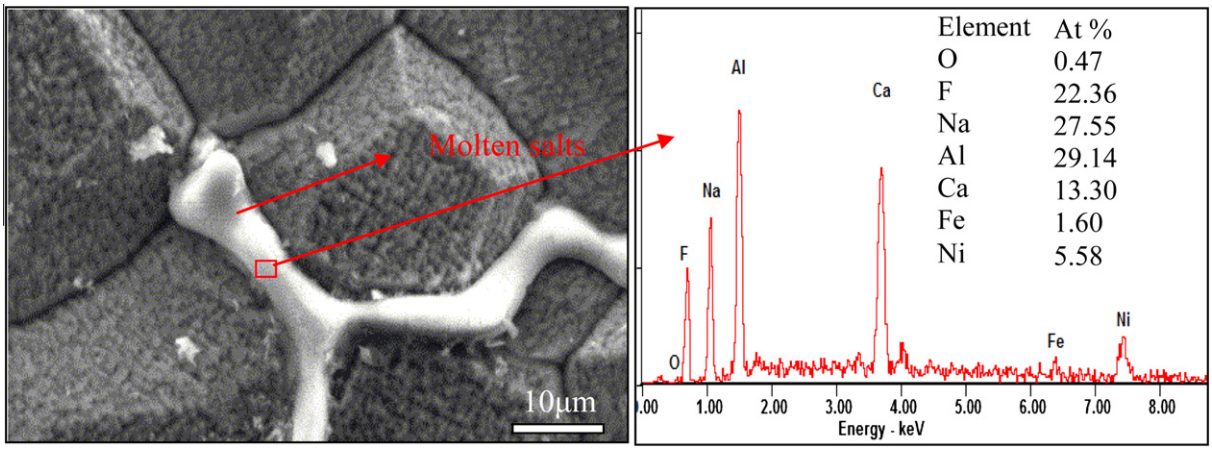

Fig. 11. A representative surface morphology and the corresponding EDX analysis of the selected region of the Ni–Fe coated specimen pre-oxidised at 1200 °C for 6 h and then corroded for 15 h at 960 °C, showing molten salts concentrated in the grain boundaries.

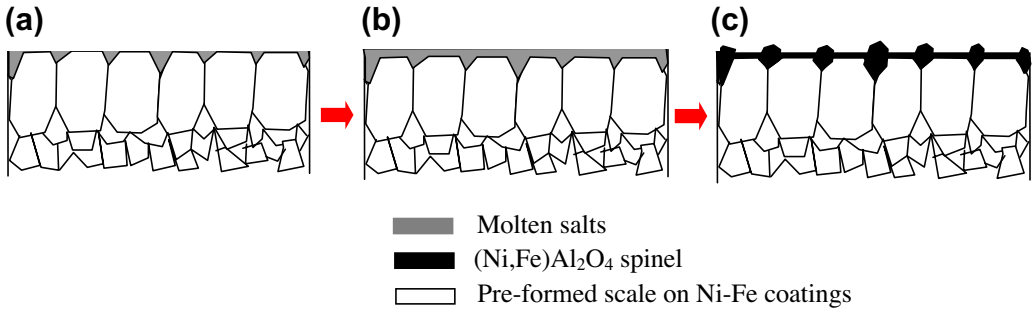

Fig. 12. Formation model of $(Ni,Fe)Al_2O_4$ spinel layer at grain boundaries and the top flat surface of pre-formed scales during hot corrosion at 960 °C: (a) molten salts are easily concentrated in the grain boundaries at the initial stage of corrosion test; (b) the mass of molten salts in the grain boundaries is larger than that on the flat surface throughout the corrosion test; (c) the morphology of the new-formed $(Ni,Fe)Al_2O_4$ spinel layer after corrosion.

According to thermodynamic data [48], for these systems, the $(Ni,Fe)Al_2O_4$ spinel is formed by the reactions (3) and (4),

$$NiO(s) + Al_2O_3(l) \rightarrow NiAl_2O_4(s) \quad (3)$$

$$FeO(s) + Al_2O_3(l) \rightarrow FeAl_2O_2(s) \quad (4)$$

The solubility of many oxides in molten salts at 1010 °C (FeO: ~5.5 wt.%, Fe_2O_3: ~0.8 wt.%, NiO: ~0.41 wt.%) has been studied by Thonstad et al. [45]. De Yong found that the solubility of Fe_2O_3 and NiO bound in $NiFe_2O_4$ were less than the individual solubilities of Fe_2O_3 and NiO respectively [47]. This is due to the added thermodynamic stability of the ferrite complex compared to the individual oxides. However, $NiFe_2O_4$ did not dissolve in stoichiometric proportions, with the Fe/Ni weight ratio in the melt ranging from 3 to 8, indicating that the solubility of iron oxides is higher than that of nickel oxide. He et al. [46] also measured the solubility of $NiFe_2O_4$ in molten salts, and found that $NiFe_2O_4$ did not dissolve stoichiometrically, and preferential dissolution of Fe in the molten salts occurred. Since the solubility of FeO in the molten salts is higher than that of Fe_2O_3 [45], it can be assumed that ferrous ions in $NiFe_2O_4$ may be more easily dissolved, compared to ferric ions in $NiFe_2O_4$. Thus, the $(Ni,Fe)Al_2O_4$ phase formation may be mainly due to the reactions (5), (3) and (4).

$$3FeO(s) + 2AlF_3(l) \rightarrow 3FeF_2(l) + Al_2O_3(l) \quad (5)[46]$$

Compared with the previously investigated Ni and pre-oxidised Ni [27], the pre-oxidised Ni–Fe coated specimen investigated in this work also exhibited much better hot corrosion resistance. After 50 h of corrosion, the highly oriented and adherent pre-formed oxide layer still existed on the specimen surface. In addition, after corrosion for 50 h, the thickness of the scale had increased only by ~40 μm compared with that of the pre-oxidised coating. Moreover, it is noted that, for the pre-oxidised coated specimen, corrosive salt was not detected in the oxide layer and substrate after the hot corrosion test. The improved corrosion resistance can be explained by following factors:

1. Both the NiO and $NiFe_2O_4$ phases, which are present in the pre-formed outer layer of the scale, are chemically inert to the molten salts [6].
2. A very dense, adherent and highly oriented oxide scale formed on the Ni–Fe coated specimen during 6 h of oxidation at 1200 °C made a significant contribution to the corrosion resistance. The scale had a graded distribution of spinel in the outer zone, so there was a high spinel content in the outer zone, which is beneficial not only to the adhesion of the scale and the electrical conductivity, but also to the resistance of hot corrosion, which inhibits the inward diffusion of oxygen and molten salts.
3. Although the molten salts were easily concentrated in the grain boundaries near the top surface, $NiFe_2O_4$ spinel particles concentrated along the grain boundaries, formed during after the pre-oxidation treatment (Figs. 5 and 6), could prevent the penetration of the salts into the scale in the initial stage of the corrosion test.

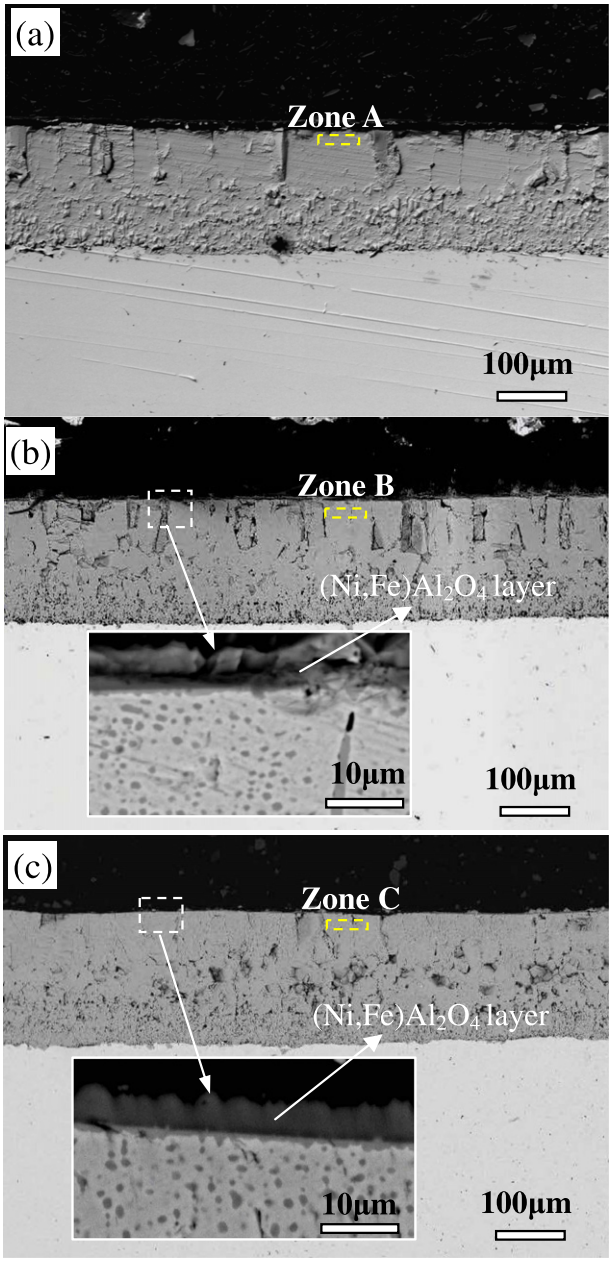

Fig. 13. SEM micrographs of the cross-section of the scale formed on the pre-oxidised Ni–Fe coated specimen during hot corrosion at 960 °C ((a): corrosion for 15 h; (b): corrosion for 30 h; (c): corrosion for 50 h). The insets show SEM images of a section of each sample at higher magnification.

4. The presence of spinel $NiAl_2O_4$ in the oxide scale also contributed to the oxidation resistance as the spinel phases usually have smaller diffusion coefficients of the cations and anions than those of their parent oxides [31]. Also, the CTE match between NiO and $NiAl_2O_4$ was improved by the incorporation of $NiFe_2O_4$ precipitates in the scale. The well-adhered oxide scale was very beneficial for protecting the substrate from hot corrosion attack. Moreover, as the corrosion process continued, although the $NiAl_2O_4$-enriched scale could be damaged due to stress, the presence of $NiFe_2O_4$ spinel particles between and in columnar the NiO grains in the subscale area (Fig. 7) could act as a second barrier to corrosion.

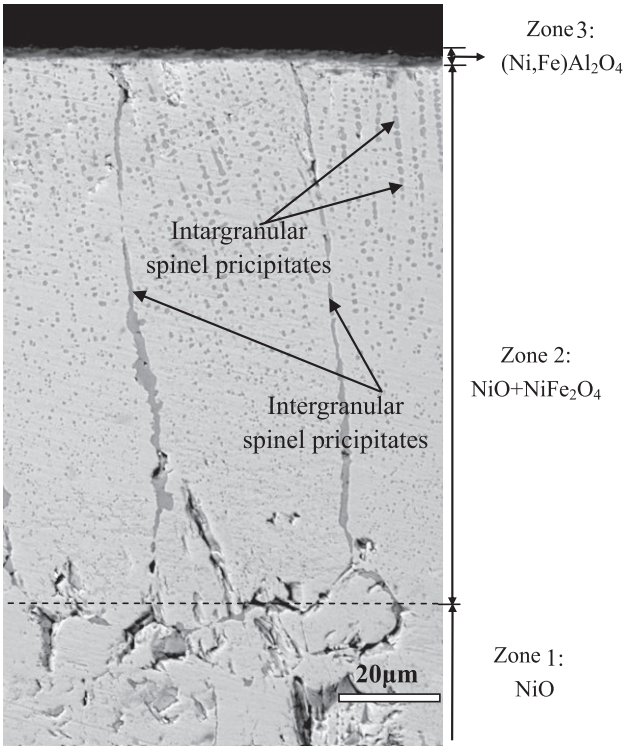

Fig. 15. Enlarged cross-section morphology of the pre-oxidised Ni–Fe coated specimen after hot corrosion at 960 °C for 50 h.

A previous investigation [27] has demonstrated that (Ni,Co)O/(Ni,Co)Fe_2O_4 composite coating thermally converted from an electrodeposited Ni–Co–Fe_2O_3 composite coating displayed better hot corrosion resistance against an Na_3AlF_6–AlF_3–CaF molten salts under standard aluminium reduction conditions, compared with bare Ni and pre-oxidised Ni. Thus, it is also worthwhile to compare the corrosion performance of these pre-oxidised Ni–Fe alloy coatings in this work with those pre-oxidised Ni–Co–Fe_2O_3 composite coatings reported in the previous work [27].

In terms of weight gains, for the pre-oxidised Ni–Fe alloy coated specimens corroded for 30 h, a lower weight gain was observed than that previously described for the pre-oxidised Ni–Co–Fe_2O_3

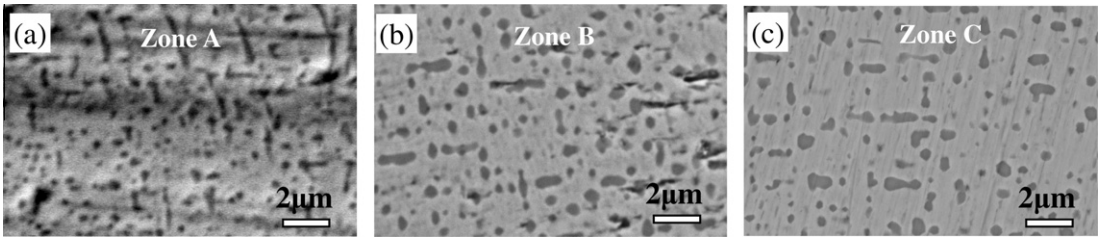

Fig. 14. The selected cross-section morphologies of the pre-oxidised Ni–Fe coated specimens after hot corrosion at 960 °C ((a): Zone A in Fig. 13(a), corrosion for 15 h; (b): Zone B in Fig. 13(b), corrosion for 30 h; (c): Zone C in Fig. 13(c) corrosion for 50 h).

coated specimens corroded for the same time. Besides, the SEM results show that the increased thickness of the NiO/$NiFe_2O_4$ composite coating after corrosion for 50 h compared with that of the pre-oxidised coating was only ~40 μm, which was similar to that of (Ni,Co)O/(Ni,Co)Fe_2O_4 composite coating after corrosion for only 30 h in the previous study [27]. What's more, these coatings were still compact after corrosion for 50 h. Thus, it can be inferred that the pre-oxidised Ni–Fe alloy coatings have a better corrosion resistance in the given environment at 960 °C, which can be attributed to their more compact and uniform structure before corrosion tests. Therefore, a Ni–Fe alloy coating seems very promising as a conductive and protective coating on Ni or steel for high temperature applications and is capable of providing long-term corrosion stability.

In addition to the hot corrosion resistance, the pre-oxidised Ni–Fe alloy coating has a unique set of properties. The XRD result (Fig. 3(b)) shows that NiO/$NiFe_2O_4$ composite coating obtained from oxidised Ni–7Fe alloy coating exhibits a high (100) orientation. In addition, the SEM results (Fig. 5) also show that the NiO/$NiFe_2O_4$ composite coating has a very smooth and dense surface. Besides, the $NiFe_2O_4$ spinels in NiO/$NiFe_2O_4$ composite coating distributed homogeneously on the surface (Fig. 5), and distributed gradiently in the cross-section (Fig. 7). What's more, the Raman (Fig. 4) and SEM results (Fig. 5) show that the spinels crystalline size is small, namely nanometre scale, whereas their number on the surface of the coating is large. Thus, the NiO/$NiFe_2O_4$ composite coating have many properties including crystalline orientation, compositional and microstructural uniformity, smooth and dense surface, crack-free form, and electrical conductivity, showing their great potential for wide applications in harsh environments.

4. Conclusions

1. A NiO/$NiFe_2O_4$ composite coating having a unique set of properties including high crystalline orientation, compositional and microstructual uniformity, smooth and dense surface, crack-free form and gradient distribution of $NiFe_2O_4$ spinel in the cross-section can be prepared by oxidised the Ni–Fe coated specimen at 1200 °C in air for 6 h.
2. The NiO/$NiFe_2O_4$ composite coating prepared by pre-oxidised Ni–Fe coating exhibits good hot corrosion resistance during 50 h exposure to molten salts at 960 °C. The reason lies mainly in that both a compact and adherent NiO/$NiFe_2O_4$ scale and intergranular $NiFe_2O_4$ spinel precipitates were formed during the oxidation treatment, which prevent the inward penetration of molten salts.

Acknowledgements

The authors would like to thank the "National Key Basic Research Programme (2005CB623703)", the "National Natural Science Foundation of China (50474051)", Innovation Foundation for Postgraduate of Hunan Province of China (CX2009B032), the "Excellent Doctor Degree Thesis Support Foundation of Central South University (2009ybfz02)" and the "Open Fund for Valuable Instrument of Central South University" for financial support, and the authors are also very grateful to Dr. Judy Hart (Ramsay memorial postdoctoral fellow in the School of Chemistry, University of Bristol) for her helpful discussion.

References

[1] V.G. Harris, A. Geiler, Y. Chen, S.D. Yoon, M. Wu, A. Yang, Z. Chen, P. He, P.V. Parimi, X. Zuo, C.E. Patton, M. Abe, O. Acher, C. Vittoria, Recent advances in processing and applications of microwave ferrites, J. Magnet. Magnet. Mater. 321 (2009) 2035–2047.
[2] H. Yin, H.P. Too, G.M. Chow, The effects of particle size and surface coating on the cytotoxicity of nickel ferrite, Biomaterials 26 (2005) 5818–5826.
[3] Y. Wang, X. Teng, J.S. Wang, H. Yang, Solvent-free atom transfer radical polymerization in the synthesis of Fe_2O_3@ polystyrene core-shell nanoparticles, Nano Lett. 3 (2003) 789–793.
[4] G.R. Dube, V.S. Darshane, Decomposition of 1-octanol on the spinel system Ga_{1-x} $Fe_x$$CuMnO_4$, J. Mol. Catal. 79 (1993) 285–296.
[5] C.V.G. Reddy, S.V. Manorama, V.J. Rao, Preparation and characterisation of ferrites as gas sensor materials, J. Mater. Sci. Lett. 19 (2000) 775–778.
[6] Z.L. Tian, Y.Q. Lai, J. Li, Y.X. Liu, Effect of Ni content on corrosion behaviour of Ni/(10NiO–90$NiFe_2O_4$) cermet inert anode, Trans. Nonfer. Met. Soc. China 18 (2008) 361–365.
[7] Y.Q. Lai, Z.L. Tian, J. Li, S.L. Ye, X.Z. Li, Y.X. Liu, Results from 100 h electrolysis testing of $NiFe_2O_4$ based cermet as inert anode in aluminium reduction, Trans. Nonfer. Met. Soc. China 16 (2006) 970–974.
[8] E. Olsen, J. Thonstad, Nickel ferrite as inert anodes in aluminium electrolysis: part I material fabrication and preliminary testing, J. Appl. Electrochem. 29 (1999) 293–299.
[9] S. Muralidharan, V. Saraswathy, L.J. Berchmans, K. Thangavel, K.Y. Ann, Nickel ferrite ($NiFe_2O_4$): a possible candidate material as reference electrode for corrosion monitoring of steel in concrete environments, Sens. Actu. B Chem. 145 (2010) 225–231.
[10] Z.H. Bi, J.H. Zhu, J.L. Batey, $CoFe_2O_4$ spinel protection coating thermally converted from the electroplated Co–Fe alloy for solid oxide fuel cell interconnect application, J. Power Sour. 195 (2010) 3605–3611.
[11] X. Montero, F. Tietz, D. Sebold, H.P. Buchkremer, A. Ringuede, M. Cassir, A. Laresgoiti, I. Villarreal, $MnCo_{1.9}Fe_{0.1}O_4$ spinel protection layer on commercial ferritic steels for interconnect applications in solid oxide fuel cells, J. Power Sour. 184 (2008) 172–179.
[12] B. Negulescu, L. Thomas, Y. Dumont, M. Tessier, N. Keller, M. Guyot, Exchange biasing in NiO/$NiFe_2O_4$ bilayers, J. Magnet. Magnet. Mater. 242–245 (2002) 529–531.
[13] S. Venzke, R.B. Van Dover, J.M. Phillips, E.M. Gyorgy, T. Siegrist, C.H. Chen, D. Werder, R.M. Fleming, R.J. Felder, E. Coleman, R. Opila, Epitaxial growth and magnetic behaviour of $NiFe_2O_4$ thin films, J. Mater. Res. 11 (1996) 1187–1198.
[14] M. Abe, Ferrite plating: a chemical method preparing oxide magnetic films at 24–100 °C and its applications, Electrochim. Acta 45 (2000) 3337–3343.
[15] T. Tsuchiya, H. Yamashiro, T. Sei, T. Inamura, Preparation of spinel-type ferrite thin films by the dip-coating process and their magnetic properties, J. Mater. Sci. 27 (1992) 3645–3650.
[16] Y.S. Chung, S.B. Park, D.W. Kang, Magnetically separable titania-coated nickel ferrite photo catalyst, Mater. Chem. Phys. 86 (2004) 375–381.
[17] J.H. Zhu, S.J. Geng, D.A. Ballard, Evaluation of several low thermal expansion Fe–Co–Ni alloys as interconnect for reduced-temperature solid oxide fuel cell, Inter. J. Hydr. Ener. 32 (2007) 3682–3688.
[18] S. Geng, Y. Li, Z. Ma, L. Wang, L. Li, F. Wang, Evaluation of electrodeposited Fe–Ni alloy on ferritic stainless steel solid oxide fuel cell interconnect, J. Power Sour. 195 (2010) 3256–3260.
[19] L. Ma, Z.Y. Li , K.C. Zhou, L. Zhang, X.P. Gan, T. Zhou, The preparations and its applications of a new composite coating, China Patent China 200910043658.X (2009).
[20] N. Shaigan, D.G. Ivey, W. Chen, Co/$LaCrO_3$ composite coatings for AISI 430 stainless steel solid oxide fuel cell interconnects, J. Power Sour. 185 (2008) 331–337.
[21] N. Shaigan, D.G. Ivey, W. Chen, Electrodeposition of Ni/$LaCrO_3$ composite coatings for solid oxide fuel cell stainless steel interconnect applications, J. Electrochem. Soc. 155 (2008) D278–D284.
[22] Q. Feng, T. Li, H. Teng, X. Zhang, Y. Zhang, C. Liu, J. Jin, Investigation on the corrosion and oxidation resistance of Ni–Al_2O_3 nano-composite coatings prepared by sediment co-deposition, Surf. Coat. Technol. 202 (2008) 4137–4144.
[23] L.M. Chang, M.Z. An, H.F. Guo, S.Y. Shi, Microstructure and properties of Ni–Co/nano-Al_2O_3 composite coatings by pulse reversal current electrodeposition, Appl. Surf. Sci. 253 (2006) 2132–2137.
[24] L. Ma, K.C. Zhou, Z.Y. Li, Synthesis of high texture orientated Ni–Co–Fe_2O_3 composite coatings by electrodeposition, in: Proceedings of the 9th Vacuum Metallurgy and Surface Engineering Conference, Beijing, 2009, pp. 231–236.
[25] L. Ma, K. Zhou, Z. Li, L. Zhang, Synthesis of (Ni,Co)Fe_2O_4-spinel coating using high temperature oxidation treatment of Ni–Co–Fe_2O_3 composite electrodeposited coating, Mater. Sci. Forum 686 (2011) 661–670.
[26] L. Ma, K.C. Zhou, Z.Y. Li, Q.P. Wei, Electrodeposition of Ni–Co–Fe_2O_3 composite coatings, J. Cent. South Univ. Technol. 17 (2010) 708–714.
[27] L. Ma, K. Zhou, Z. Li, Hot corrosion of a novel (Ni,Co)O/(Ni,Co)Fe_2O_4 composite coating thermally converted from an electrodeposited Ni–Co–Fe_2O_3 composite coating, Corros. Sci. 53 (2011) 2357–2367.
[28] H.Q. Li, F. Ebrahimi, An investigation of thermal stability and microhardness of electrodeposited nanocrystalline nickel-21% iron alloys, Acta Mater. 51 (2003) 3905–3913.
[29] P. Fricoteaux, C. Rousse, Influence of substrate, pH and magnetic field onto composition and current efficiency of electrodeposited Ni–Fe alloys, J. Electroanal. Chem. 612 (2008) 9–14.
[30] L. Ma, K. Zhou, Z. Li, Oxidation behaviours of electrodeposited Nickel–iron coatings at 900–1200 °C in air, unpublished data.

[31] A.D. Dalvi, W.W. Smeltzer, The kinetics and morphological development of the oxide scale on Nickel–Iron Alloys (0–25 w/o Fe) at 1000 °C, J. Electrochem. Soc. 118 (1971) 1978–1985.
[32] J.H. Kim, I.S. Hwang, Development of an in situ Raman spectroscopic system for surface oxide films on metals and alloys in high temperature water, Nuc. Eng. Des. 235 (2005) 1029–1040.
[33] G. Calvarin, A.M. Huntz, A.H.l. Goff, S. Joiret, M.C. Bernard, Oxide scale stress determination by Raman spectroscopy application to the $NiCr/Cr_2O_3$ system and influence of yttrium, Script. Mater. 38 (1998) 1649–1658.
[34] Y.L. Liu, H. Wang, Y. Yang, Z.M. Liu, H.F. Yang, G.L. Shen, R.Q. Yu, Hydrogen sulfide sensing properties of $NiFe_2O_4$ nanopowder doped with noble metals, Sens. Actu. B Chem. 102 (2004) 148–154.
[35] J. Birnie, C. Craggs, D.J. Gardiner, P.R. Graves, Ex situ and in situ determination of stress distributions in chromium oxide films by Raman microscopy, Corros. Sci. 33 (1992) 1–12.
[36] M.A. Rhamdhani, P.C. Hayes, E. Jak, Subsolidus phase equilibria of the Fe–Ni–O system, Metal. Mater. Trans. B 39 (2008) 690–701.
[37] S.R. Summerfelt, C.B. Carter, Dissolution of $NiFe_2O_4$ particles in a NiO matrix, Acta Metal. Mater. 40 (1992) 2799–2804.
[38] K.M. Ostyn, C.B. Carter, M. Koehne, H. Falke, H. Schmalzried, Internal reactions in oxide solid solutions, J. Am. Ceram. Soc. 67 (1984) 679–685.
[39] A.D. Dalvi, W.W. Smeltzer, A Diffusion Model for Oxidation of Nickel–Iron Alloys at 1000 °C, J. Electrochem. Soc. 121 (1974) 386–394.
[40] A.D. Dalvi, W.W. Smeltzer, Thermodynamics of the Iron–Nickel–Oxygen system at 1000 °C, J. Electrochem. Soc. 117 (1970) 1431–1436.
[41] C.F. Windisch Jr., K.F. Ferris, G.J. Exarhos, Synthesis and characterisation of transparent conducting oxide cobalt–nickel spinel films, J. Vac. Sci. Technol. A 19 (2001) 1647–1651.
[42] A. Petric, H. Ling, Electrical conductivity and thermal expansion of spinels at elevated temperatures, J. Am. Ceram. Soc. 90 (2007) 1515–1520.
[43] A.J. Ardell, Quantitative predictions of the trans-interface diffusion-controlled theory of particle coarsening, Acta Mater. 58 (2010) 4325–4331.
[44] G.P. Wirtz, M.E. Fine, Precipitation and coarsening of magnesioferrite in dilute solutions of Iron in MgO, J. Am. Ceram. Soc. 51 (1968) 402–406.
[45] J. Thonstad, P. Fellner, G.M. Haarberg, J. Híveš, H. Kvande, Å. Sterten, Aluminium Electrolysis, third ed., Aluminium-Verlag, Düsseldorf, Germany, 2001.
[46] H.B. He, Densification, electrical conductivity and corrosion behaviour of $NiFe_2O_4$–10NiO based ceramic anode for aluminium electrolysis, in: Doctor thesis, Central South University, Hunan, China, 2010.
[47] D.H. DeYoung, Solubilities of oxides for inert anodes in cryolite-based melts, in: R.E. Miller (Ed.), Light Metals, TMS, Warrendale, PA, 1986, pp. 299–307.
[48] I. Barin, Thermodynamical Data of Pure substances, third ed., VCH Verlagsgesellschaft Gmb-H, D-69451, Weinheim, Germany, 1995.